Partitioning of sensible and latent heat fluxes in different vegetation types and their spatiotemporal variations based on 203 FLUXNET sites

Huiqing Lin[1,2], Yan Li[1,2*], Lei Zhao[3,4]

1. State Key Laboratory of Earth Surface Processes and Resources Ecology, Beijing Normal University, Beijing 100875, China

2. Institute of Land Surface System and Sustainable Development, Faculty of Geographical Science, Beijing Normal University, Beijing 100875, China

3. Department of Civil & Environmental Engineering, University of Illinois at Urbana-Champaign, Urbana, IL, 61801, USA

4. National Center for Supercomputing Applications, University of Illinois at Urbana-Champaign, Urbana, IL, 61801, USA

*Correspondence: yanli.geo@gmail.com

Key points

1. Analyzed the spatiotemporal variations of Bowen ratio among 12 vegetation types based on 203 FLUXNET sites

2. The spatiotemporal variations in Bowen ratio can be explained by climatic, geographical, and biological factors, especially climate factors

3. Open shrublands showed the highest Bowen ratio, followed by shrubs, savannas, grasslands, forests, croplands and wetlands

Abstract

Bowen ratio reflects the partitioning between sensible and latent heat fluxes and plays a crucial role in land-atmosphere interaction. In this study, the spatiotemporal variations of Bowen ratio among 12 vegetation types were analyzed using observations from 203 FLUXNET sites worldwide and compared against Community Land Model. Results showed that the annual mean Bowen ratio across all sites was 1.48 ± 1.20 (mean ± SD). Sites with Bowen ratios less than 1 (39%, 80 sites) were found across all continents, and the ones with higher Bowen ratios (>3)(7%, 14 sites) appeared in dry and warm areas. Open shrublands showed the highest Bowen ratio (3.04 ± 0.58), whereas wetlands showed the lowest (0.74 ± 0.09). In terms of seasonality, Bowen ratio showed a U-curve with lower values in local summer and higher in spring and autumn in the northern hemisphere; the opposite occurred in the southern hemisphere. The spatiotemporal variations in Bowen ratio can be explained by climatic, geographical, and biological factors, with climate factors having the greatest impact. Bowen ratio increased under higher VPD (R = 0.45) and hotter (R=0.14) conditions with more shortwave radiation (R=0.39), and decreased with higher precipitation (R=-0.34), albedo (R=-0.16), and leaf area index (R=-0.25). CLM well reproduced the global annual mean Bowen ratio, but showed larger differences for certain vegetations types such as open shrublands (-1.51), woody savannas (+0.98). Our results could enhance our understanding of biotic and environmental controls on land surface energy fluxes and help improve land surface and climate models.

Keywords: Bowen ratio, sensible heat, latent heat, vegetation, FLUXNET, Community Land Model

1. Introduction

The energy exchange between the land and the atmosphere plays an important role in the biogeochemical cycle, water cycle, and climate change (Zeng et al., 2020; Qiu et al., 2021; Foley

et al., 2003). In particular, vegetation covering 70% of the earth's land surface modulates how net radiation at the land surface is balanced by sensible heat, latent heat, and soil heat flux and thus has a strong impact on land-atmosphere interaction (Zhang et al., 2019; Su et al., 2021; Gray et al., 2018; van Heerwaarden and Teuling, 2014). Vegetation differences in type, structure, and density affect surface energy partitioning (Burakowski et al., 2018; Nicholls and Carey, 2021; Cho et al., 2011; Jo et al., 2004). In terms of radiative processes, vegetation coverage could increase land surface roughness and decrease albedo (Pang et al., 2022), leading to an increase in net radiation. In terms of non-radiative processes, vegetation could increase evapotranspiration, leading to an increase in latent heat and a decrease in sensible heat (Duveiller et al., 2018). Both radiative and non-radiative changes associated with vegetation can influence land-atmosphere interaction and the climate (Bonan, 2008).

Bowen ratio, defined as the ratio of sensible to latent heat fluxes at a certain interface, is often used to characterize their partitioning (Bowen, 1926). A large Bowen ratio indicates the turbulent heat flux is dominated by sensible heat, whereas a small ratio suggests the dominance of latent heat. Bowen ratio and aerodynamic resistance jointly affect surface temperature through the non-radiative process (Rigden and Li, 2017; Su et al., 2021; Lee et al., 2011). The greater sensible heat associated with a higher Bowen ratio leads to increased land surface temperature and aggravated drought (McGloin et al., 2019). Moreover, Bowen ratio is strongly regulated by climate and vegetation conditions (Ping et al., 2018; Tang et al., 2014; Gholz and Clark, 2002). For example, it is reported that grassland could decrease Bowen ratio through increased latent heat to suppress heatwave compared to forests, but this process accelerated soil moisture depletion and induced a critical shift in the regional climate system that leads to increased heating (Teuling et al., 2010). Given the importance of vegetation modulation, it is meaningful to investigate how Bowen ratio differs among different vegetation types and explore its controlling factors.

Bown ratio and its climatic effects were primarily studied through site measurement and modeling (Wang and Dickinson, 2012; Lee et al., 2011). It is found that Bowen ratio was generally high in drier areas (e.g., > 5 in desert and semi-arid areas), and low in moist areas (e.g., 0.5~0.2 in tropical rain forests and irrigated croplands) (Oke and Cleugh, 1987; Morwal et al., 2016; Ryu et al., 2008; Juang et al., 2007). Vegetation changes are often accompanied by surface energy fluxes and Bowen ratio changes. Deforestation tended to elevate Bowen ratio and warm the land surface since forests had a lower Bowen ratio (Yuan et al., 2021; Lee et al., 2011). However, most of these observation-based assessments focused on a certain geographic region with relatively few global-scale studies (Wilson et al., 2002). In addition, surface fluxes are routinely simulated by land surface and climate models, but models have known biases in their energy partitioning between sensible and latent heat that affect their performance (Boisier et al., 2012; Meier et al., 2018; Chen et al., 2018). The latent heat partitioning within different land-cover types was diagnosed to be a major uncertainty source for the different climate responses to land cover change in a model comparison project (Boisier et al., 2012). In another study, the biases of Community Land Model (CLM) in simulating daily minimum land surface temperature were linked to underestimated latent heat for broadleaf deciduous trees and crops while overestimated for non-arctic grasses and broadleaf evergreen trees (Meier et al., 2018). Given the essential role of latent/sensible heat fluxes in heat and water cycling, it is also necessary to evaluate their partitioning in land surface/climate models based on the most updated observation data.

In this study, we quantified the Bowen ratio of 12 vegetation types based on the up-to-date observations from 203 FLUXNET sites, and analyzed the factors that drive the spatiotemporal variations of Bowen ratio. We further compared the CLM modeled Bowen ratio with these FLUXNET observations to evaluate the model performance. This work provides a basis for

understanding the important role of vegetation in land-atmosphere interaction and climate through a focus on energy partitioning.

2. Methods and data

2.1 Fluxnet and satellite data

The flux data from FLUXNET, a global network of flux observation sites (Fig 1 and Supplementary Table 1) (https://fluxnet.org/) were used in this study. The FLUXNET2015 Dataset (accessed by 2021.1.30) provides continuous measurements of carbon and energy fluxes at half-hourly to hourly time intervals by eddy covariance method (Baldocchi et al., 2001; Ma et al., 2021). Flux sites can be classified into 12 vegetation types based on the MODIS IGBP (International Geosphere Biosphere Programme) land cover classification (Fig 1a), including evergreen needleleaf forests (ENF, N=44), evergreen broadleaf forests (EBF, N=15), deciduous needleleaf forests (DNF, N=1), deciduous broadleaf forests (DBF, N=25), mixed forests (MF, N=9), closed shrublands (CSH, N=3), open shrublands (OSH, N=11), woody savannas (WSA, N=6), savannas (SAV, N=9), grasslands (GRA, N=39), wetlands (WET, N=21), and croplands (CRO, N=20). These sites are distributed across major climate regions (tropical, subtropical, temperate, and cold zones) and continents (Asia, Africa, North America, South America, and Oceania, especially Europe and North America). Fig 1b shows the distribution of 203 flux sites with their site temperature and precipitation in the climate space of the land surface (the shading area). Most of the climate space of earth's land was covered by the FLUXNET sites, indicating good representativeness of the world's vegetation.

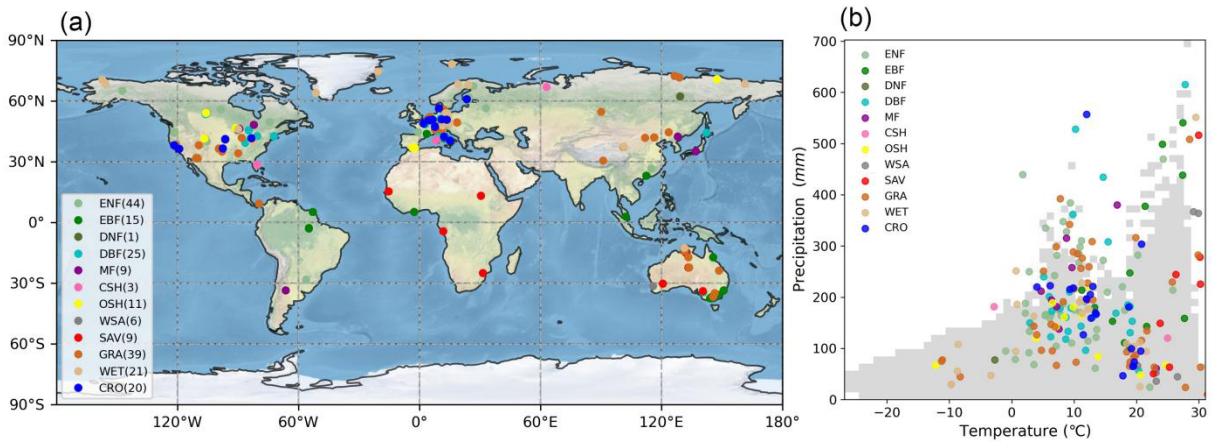

Figure 1. (a) Spatial distribution of global FLUXNET sites with their corresponding vegetation types. Numbers in parentheses denote the number of sites for different vegetation types; (b) The 203 sites in the climate space defined by their annual mean temperature and precipitation. The gray areas denote the climate space over the land (data source: CRU TS Version 4.05).

We used sensible heat (H_F_MDS) and latent heat (LE_F_MDS) from FLUXNET to estimate Bowen ratio at each site and obtained environmental factors including precipitation (P_F), temperature (TA_F), vapor pressure deficit (VPD_F), incoming shortwave radiation (SW_IN_F), and incoming longwave radiation (LW_IN_F). Albedo was calculated as the outgoing shortwave radiation (SW_OUT) divided by the incoming shortwave radiation (SW_IN_F). Since fluxes measured by eddy covariance at night have missing data and large errors (Mahrt, 1999; Yuan et al., 2021), we used the gap-filled half-hourly data of these variables and extracted only the daytime data. Daytime was defined as the local time from 9:00 to 16:00 (McGloin et al., 2019; Yuan et al., 2021). Then we removed data values below 5% and above 95% for sensible and latent heat fluxes to reduce the influence of outliers on the half-hourly scale. At each site, only the site years with available data more than 35% of all the daytime half-hour periods were kept for further analysis (Wilson et al., 2002). Finally, 203 sites were retained. These half-hourly data (e.g., sensible and latent heat) were averaged to monthly scale, and the multi-year mean Bowen ratio was calculated by dividing sensible heat by latent heat at either monthly or annual scales.

Leaf area index (LAI) data of each site were obtained from MODIS LAI product (MCD15A3H.006 MODIS Leaf Area Index/FPAR 4-Day Global 500m) from 2000 to 2020 via Google Earth Engine. The multi-year annual mean LAI was extracted at each site location.

To analyze the factors influencing spatiotemporal variations in Bowne ratio, we conducted linear regression analyses between Bowen ratio and climatic (precipitation, vapor pressure deficit, temperature, shortwave radiation, longwave radiation, and albedo), geographical (latitude and longitude), and biological factors (LAI).

2.2 Model simulation data from CLM

Community Land Surface Model 5.0 (CLM 5.0) is the most recent part of the land surface component of the Community Earth System Model, and has been widely used in climate, hydrology, and ecology research (Lawrence et al., 2019). In this study, an offline simulation by CLM 5.0 with prescribed satellite phenology and the separate soil column configuration (Meier et al., 2018; Schultz et al., 2016) was conducted at the spatial resolution of 0.5° from 2001 to 2015, driven by a revised climatology GSWP3 (the Global Soil Wetness Project Phase3) as the atmospheric forcing (http://hydro.iis.utokyo.ac.jp/GSWP3/). The years 2001 to 2005 were treated as spinup periods, and only years from 2006 to 2015 were used in our analysis. The hourly subgrid output data from CLM were processed in the same way as the FLUXNET data, including extracting daytime data (9:00-16:00) and removing outliers (5% and 95%) in each plant functional types (PFT). Because CLM5.0 model uses PFT to classify vegetation, while FLUXNET uses IGBP, we created a look-up table to convert them (Supplementary Table 2). When comparing with FLUXNET, we extracted CLM subgrid output based on the location (by longitude and latitude) and PFT of 203 sites, and then calculated Bowen ratio. In order to explore the relationship between Bowen ratio and environmental factors, regression analyses were conducted with environmental data of CLM5.0.

3. Results

3.1 Spatial variations of Bowen ratio

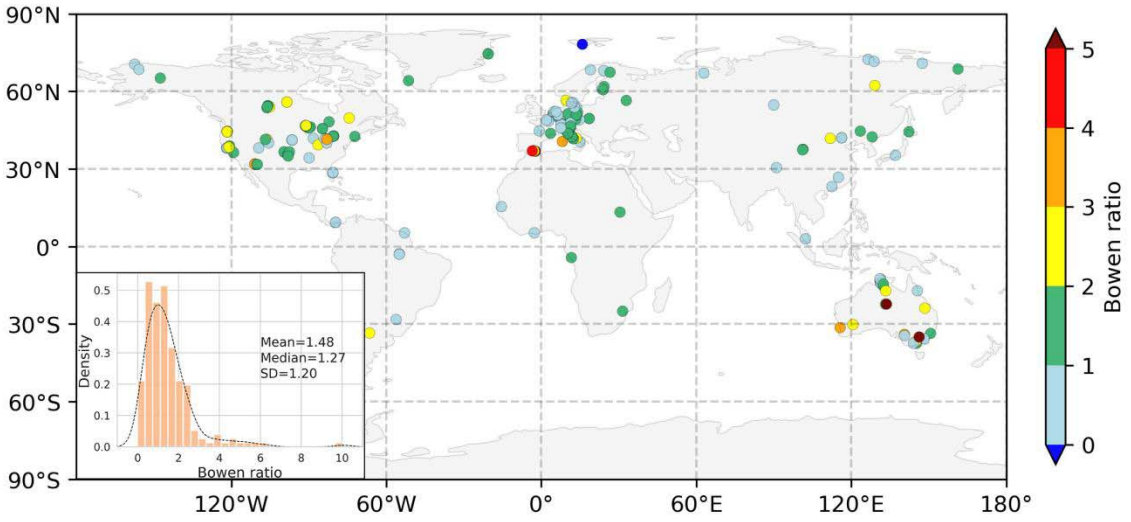

Figure 2. Spatial distribution of multi-year annual mean Bowen ratio across 203 FLUXNET sites and their frequency distribution (inset).

At the annual scale, the multi-year mean Bowen ratio of all sites was averaged to be 1.48 ± 1.20 (mean ± SD)(Fig 2). Such a larger-than-one Bowen ratio indicated that globally, sensible heat dominated the turbulent fluxes exchanged between the land and the atmosphere. Of all 203 sites, about 61% sites (123) had Bowen ratio greater than 1. Higher Bowen ratio (>3)(7%, 14 sites) appeared in middle latitude sites, especially in North America and Australia (Fig 2). The 39% sites (80) with Bowen ratio below 1 were found on all continents ranging from about 30°S to 70°N (except Antarctica with no site). From the Köppen climate classification (Peel et al., 2007), sites with high Bowen ratios (>1) usually appeared in the arid desert (BW) and arid steppe (Bs) climate (Fig S1), and those sites with smaller Bowen ratio (<1) were usually located in warm temperate and humid climate (Cf). Despite this general pattern, Bowen ratio showed considerable differences within similar climate regimes (e.g., in warm temperate and fully humid climate), reflecting the modulation role of vegetation.

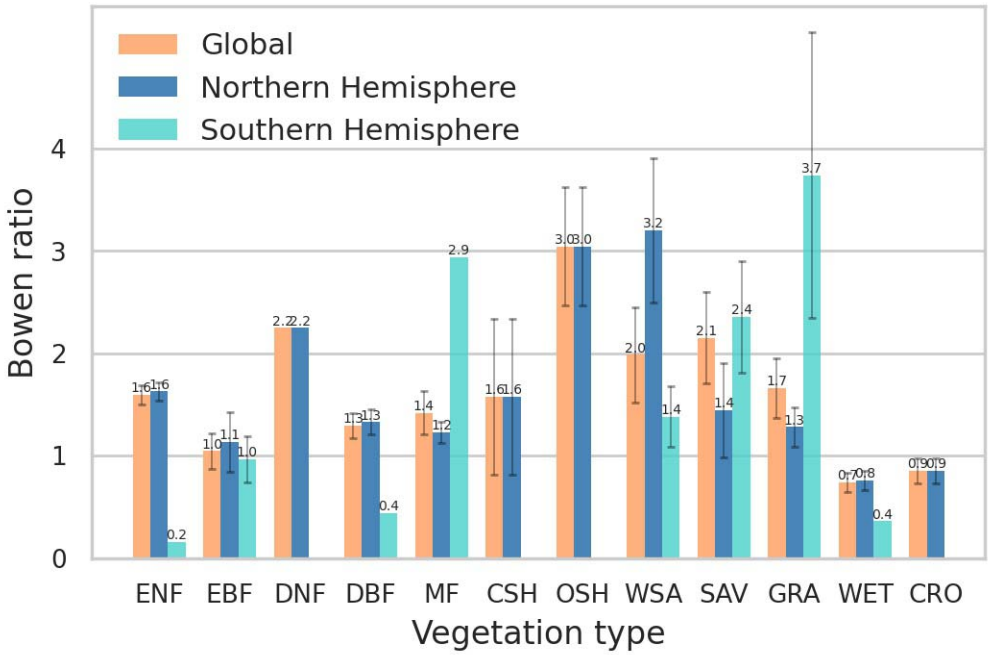

Figure 3. The multi-year annual mean Bowen ratio of different vegetation types based on FLUXNET across the globe, in the northern and southern hemispheres. The error bar on each bar represents standard error.

We found that Bowen ratio was significantly different among different vegetation types (Fig 3). Globally, open shrublands (3.04±0.58) and savannas (2.15±0.45 for SAV, 1.98 ± 0.46 for WSA) had the highest Bowen ratio among all vegetation types. This was followed by forest vegetation types including deciduous needleleaf forests (2.25), evergreen needleleaf forests (1.59±0.09), and mixed forests (1.42±0.21). Croplands (0.85±0.13) and Wetlands (0.74±0.09) had the smallest Bowen ratio among all vegetation types.

We noticed that even for the same vegetation type, Bowen ratio varied substantially in the northern (NH) and southern hemispheres (SH). This reflected the environmental differences in their climate, radiation, topography, and other aspects (Fig 3and Fig S2). For example, Bowen ratio of most vegetation types was greater than 1; however, evergreen needleleaf forests, deciduous broadleaf forests, and wetlands in the SH with high precipitation (Fig S2) had Bowen

ratio <1. There were also considerable differences in Bowen ratio of grassland between hemispheres (3.74±1.34 in SH vs. 1.28±0.19 in NH) (Fig S2). This could be explained by the fact that grassland sites in the SH were mainly located in arid steppe areas, characterized by high temperature, VPD, and radiation, while grassland sites in the NH were found in low temperature and high precipitation areas (Fig S2).

3.2 Seasonal variations of Bowen ratio

Bowen ratio of different vegetation types had distinct seasonal variations in the NH and SH. Most vegetation in the NH showed U-shaped seasonal variations in Bowen ratio (Fig 4), with small values in local summer and large values in local spring and autumn. However, in the SH, many vegetation types including deciduous broadleaf forests, mixed forests, woody savannas, savannas, and grasslands showed an inverted U-curve, with larger Bowen ratios in local summer but lower in spring and autumn. These patterns might be related to their different climate seasonalities. The high temperature and high precipitation typically coincided in summer in the NH, during which vegetation growth peaked with the largest evapotranspiration (ET), thereby leading to the lowest Bowen ratio. By contrast, most sites in the SH experienced less precipitation at local summer for SH, which limited ET and increased Bowen ratio (Fig S3). It is worth noting that Bowen ratio values had a larger bias in winter. This was caused by the FLUXNET data uncertainty in winter when the energy balance closure issues occurred, especially for evergreen needleleaf forests, mixed forests, deciduous broadleaf forests, and wetlands (Cui and Chui, 2019).

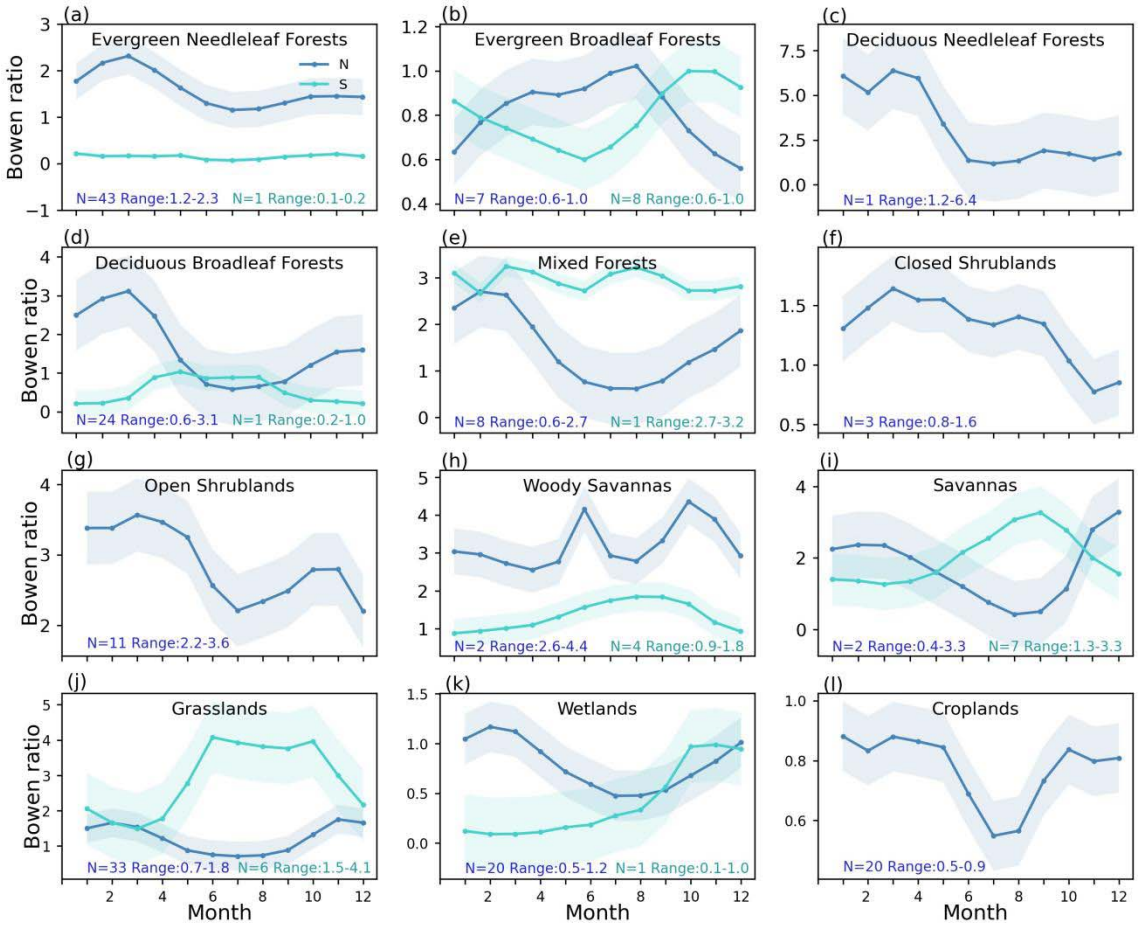

Figure 4. Seasonal variations of Bowen ratio of different vegetation types in the northern (blue) and southern (cyan) hemisphere based on FLUXNET. The seasonality of SH was shifted by 6 months to align it with NH. The shading area represents one standard deviation. Note that the display ranges of the Y-axis are different in each panel to highlight fluctuation.

3.3 Climatic, geographical, and biological drivers for Bowen ratio

In order to explore the factors influencing the spatial variations of Bowen ratio, we conducted regression analyses between annual mean Bowen ratio and several climatic, geographical, and biological factors (Fig 5 and Fig S2). Among them, climate factors had the largest impact on Bowen ratio. Vapor pressure deficit ($R=0.45$, $p<0.001$), incoming shortwave radiation ($R=0.39$, $p<0.001$), and temperature ($R=0.14$, $p<0.05$) showed positive correlations with Bowen ratios,

whereas precipitation ($R=-0.34$, $p<0.001$), albedo ($R=-0.16$), and incoming longwave radiation ($R=-0.04$) showed negative correlations. These results suggested that Bowen ratio became higher under dry/drought and hot conditions (e.g., high VPD, temperature, and less precipitation).

Since temperature and precipitation are compounded, we made regressions separately for dry (precipitation<10mm/month) and wet sites (precipitation>30mm/month) to explore the central role of precipitation/moisture in determining energy partitioning because they modulate the temperature effects (Fig S4). The high Bowen in dry sites reflected that sensible heat is the preferred way of heat transfer when evaporation is limited. In this case, Bowen ratio increased with temperature due to a sharp increase of sensible heat with temperature (Fig S4 a). At wet sites with sufficient precipitation/moisture, heat tended to be transferred in the form of latent heat. Therefore, Bowen ratio decreased with the temperature increase due to promoted latent heat with increased temperature (Fig S4 b).

In terms of geographical factors, longitude showed no apparent correlations with Bowen ratio. For latitude, Bowen ratio increased with the increasing latitude in the SH ($R= -0.18$) but not in the NH ($R=-0.07$). As for the biological factor, there was a significant negative relationship between LAI and Bowen ratio ($R=-0.25$, $p<0.001$), revealing the important pathway by which vegetation regulates Bowen ratio. A larger LAI of vegetation effectively increased latent heat through higher ET (Fig S5), while sensible heat remained stable (Fig S6), leading to decreased Bowen ratio. It is worth noting that although sensible heat (Fig S6) and latent heat (Fig S5) showed significant relationships with almost all environmental factors, their strong relationships with environmental factors were weakened in Bowen ratio, reflecting the different responses of sensible and latent heat fluxes to environment factors.

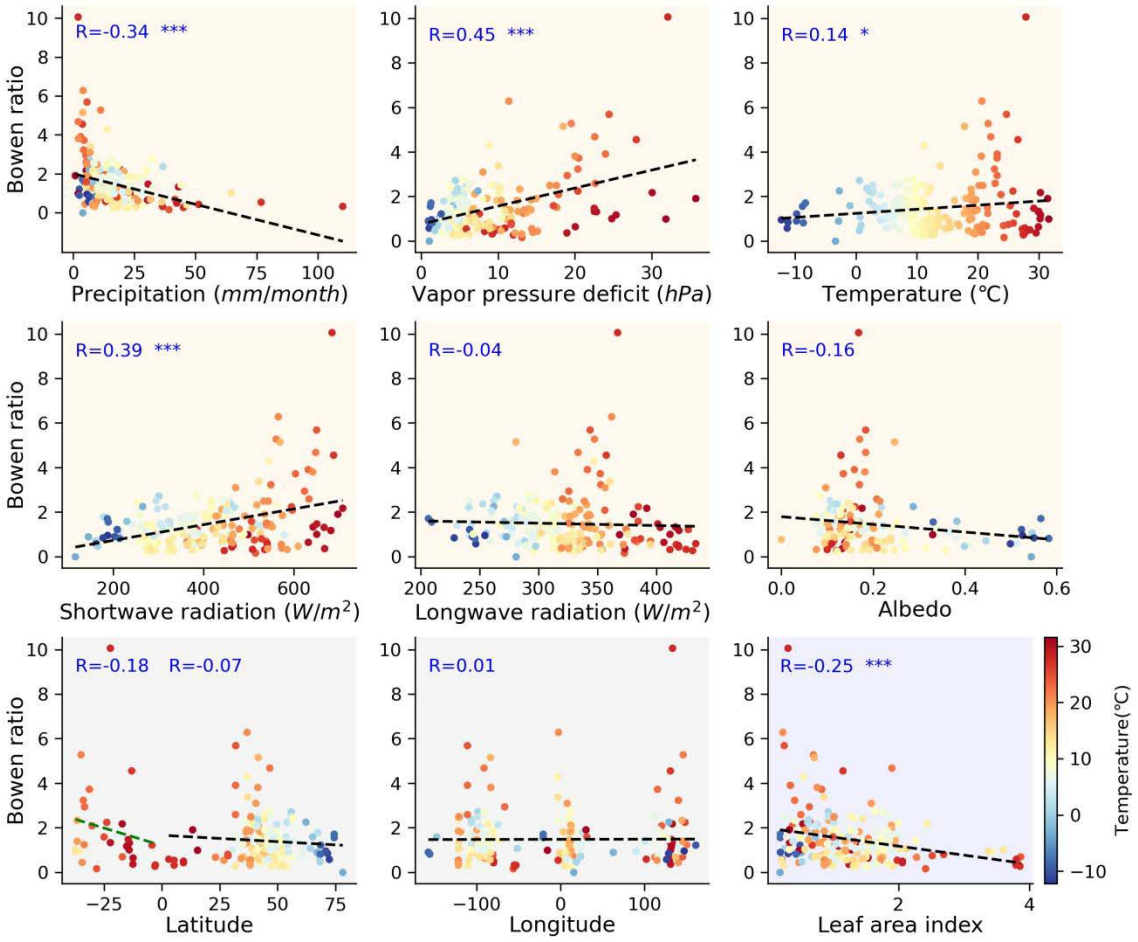

Figure 5. The spatial relationship between Bowen ratio and different climatic (orange background), geographical (gray), and biological factors (blue) based on FLUXNET data. Each dot represents a site and the dashed lines show the regression line. R is Pearson correlation coefficient with asterisks denoting significance levels (*for $p<0.05$; **$p<0.01$, and ***for $p<0.001$). The color of data points shows the mean temperature.

3.4 Comparing Bowen ratio between FLUXNET observations and CLM simulation

We extracted sensible and latent heat fluxes from the subgrid output CLM simulation at the location of flux sites with the same PFT (plant functional types) to enable comparison with FLUXNET observations (Fig 6). Globally, CLM had relatively good performance in simulating sensible heat ($R=0.69$, $P<0.001$), latent heat ($R=0.69$, $P<0.001$), and to a less extent for Bowen

ratio (R=0.42, P<0.001)(Fig 6 a-c). The simulated sensible heat and latent heat from CLM were 106.18 W/m2 and 88.14 W/m2 averaged at flux site locations, respectively, resulting in a global mean Bowen ratio of 1.42. In comparison, the corresponding values from FLUXNET data were 110.03 W/m2, 88.60 W/m2, and 1.54, respectively. Therefore, CLM showed a smaller global mean Bowen ratio by 0.12 relative to FLUXNET observations.

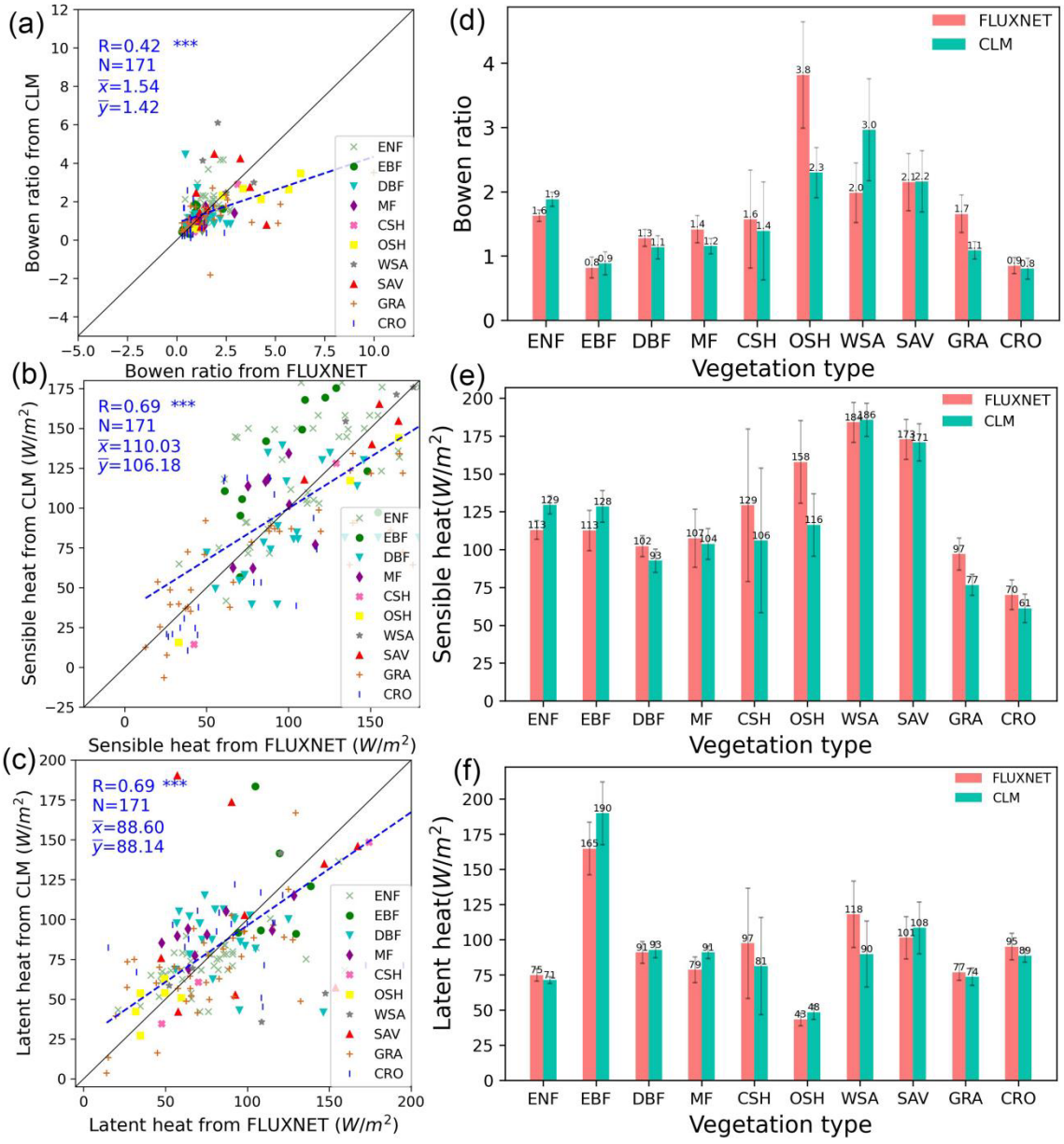

Figure 6. Comparison of annual mean (a) Bowen ratio, (b) sensible heat (H) and (c) latent heat(LE) between CLM model simulation and FLUXNET observations. The black line denotes

the 1:1 line. The right column shows the comparison of (d)Bowen ratio,(e)sensible heat (H), and (f)latent heat (LE) between CLM simulation and FLUXNET data in different vegetation types. Since there is no DNF (1) and WET (21) in the model, they were excluded. The H and LE values of some sites in CLM were missing, so the number of points used for analysis is 171. Note: DNF and WET were excluded due to null values in CLM simulation results.

Although CLM can well simulate the annual mean Bowen ratio at the global scale, there were large discrepancies when compared with FLUXNET for different vegetation types (Fig 6d). The largest differences appeared in open shrublands where CLM (2.30±0.39) simulated a much smaller Bowen ratio than in FLUXNET (3.81±0.83), yielding an underestimation of 1.51. Similar underestimation was found for grasslands (GRA, 1.09±0.14 for CLM vs 1.65±0.08 for FLUXNET). However, woody savannas (WSA, 2.96±0.79 for CLM vs. 1.98±0.46 for FLUXNET) and evergreen needleleaf forests (ENF, 1.88±0.11 for FLUXNET vs. 1.62± 0.08 for FLUXNET) from CLM showed a strong overestimated Bowen ratio than observations. The differences in Bowen ratio for the rest vegetation types ranged from 0.3 to 0.1. These differences in Bowen ratio between CLM and FLUXNET originated from multiple combinations of the differences between simulated sensible and latent heat fluxes. For example, a lower simulated Bowen ratio could be caused by either a much smaller sensible heat (e.g., GRA and croplands/CRO), or a larger latent heat relative to the other (e.g., open shrublands/OSH, deciduous broadleaf forests/DBF, and mix forests/MF). A larger simulated Bowen ratio could be caused by the opposite combination with a higher sensible heat (e.g., evergreen needleleaf forests/ENF). Therefore, Bowen ratio with small differences could reflect the canceling of biases in sensible and latent heat if their biases went to the same direction.

4. Discussion

In this study, the updated data of 203 FLUXNET sites were used to estimate Bowen ratio to analyze the partitioning of surface turbulent heat fluxes. We found that Bowen ratio was positively correlated with vapor pressure deficit, temperature, and incoming shortwave radiation and negatively correlated with precipitation, albedo, and leaf area index. This verifies that Bowen ratio depends on the differences in heat and water exchanges between land and atmosphere. Under climate conditions with high temperatures and sufficient precipitation, heat prefers to exist as latent heat. When water is limited (ET is limited), heat can only exist as sensible heat, leading to a higher Bowen ratio (Fig S5 and Fig S6). Therefore, Bowen ratio is generally high in arid and hot areas but low in humid regions (Bateni and Entekhabi, 2012; Zhao et al., 2018). Among vegetation types, forests have larger LAI and lower albedo and thus absorb more solar radiation. Also, more developed roots of forests enable absorbing deep water to maintain ET, especially during dry periods. Therefore, forests have high efficiency to move water from the land surface to the atmosphere via ET/latent heat (Lawrence et al., 2022). In contrast, grassland has smaller LAI and shallow roots, which limits the ET, leading to greater sensible heat and a larger Bowen ratio. The multi-year annual mean Bowen ratio in grasslands (1.66±0.29) was higher than most forest types (Fig 3), and it also showed large seasonal variations of 1.50-4.07 in the southern hemisphere (Fig 4j). As for wetlands and croplands, the former is usually located in humid areas, while the latter is under intensive human management which might be affected by irrigation. For these reasons, they had the lowest Bowen ratios among all vegetation types and showed small seasonal variations (0.28-1.08 for wetlands and 0.55-0.88 for croplands) (Fig 4).

The FLUXNET data provide observations for analyzing the spatiotemporal variations in Bowen ratio of all vegetation types and a useful benchmark for evaluating the accuracy of the model. However, the differences between FLUXNET and CLM of different vegetation types could be linked to several other factors. First, FLUXNET site data are measured by the eddy covariance method. The measurement error and the energy closure problem could influence the estimation of

309 Bowen ratio (Wilson et al., 2002). Second, there is a scale mismatch between FLUXNET site and
310 CLM model grid. The CLM model grid of 0.5° resolution is too coarse to represent the
311 heterogeneous FLUXNET site conditions. Besides, different time periods between FLUXNET
312 (varying across sites, Supplementary Table 1) and CLM data (10 years, from 2006 to 2015) also
313 contribute to the differences in Bowen ratio. Third, the land cover classification of CLM is
314 different from FLUXNET, which might introduce inconsistency as each PFT has its own
315 parameters in the model. Finally, CLM itself has uncertainty in the representations of the energy
316 and hydrological processes, causing biases in ET and soil moisture (Deng et al., 2020; Gao et al.,
317 2021). In our study, we focused on assessing the performance of CLM 5.0 but did not investigate
318 the specific causes in the modeling processes. More improvements in land surface models are
319 needed to resolve this difference in the future.

320 We acknowledge limitations in our analyses of data sampling and calculation. Although selected
321 flux sites are distributed in most climate regions (Fig 1b), not all lands are equally sampled (e.g.,
322 extremely dry and cold regions are undersampled). To further investigate the spatial sampling
323 issues, we used CLM5.0 data covering all land grids to repeat the regression analyses between
324 Bowen ratio and influencing factors (Fig S7). It can be found that most fitting relationships in
325 CLM were consistent with FLUXNET results in sign, which confirms the general reliability of
326 regression analyses at the site level. However, albedo showed a positive correlation with Bowen
327 ratio ($R=0.45$, $p<0.001$), in contrast to the negative correlation obtained with FLUXNET ($R=-$
328 0.16, $p>0.05$). When we restricted the regression analyses of the CLM results to flux site
329 locations only (Fig S8), a negative relationship between albedo and Bowen ratio appeared and
330 was in line with the FLUXNET results (Fig 5). This demonstrated that the uneven spatial
331 sampling of FLUXNET data might bias the analyses for spatiotemporal variations in Bowen ratio.
332 In addition, we found that the estimation of Bowen ratio was highly sensitive to specific choices
333 in the data processing procedures. For example, the treatment of outliers, the different ways to

define daytime (local time or incoming shortwave radiation threshold), and the time scale at which the ratio was calculated would lead to slightly different Bowen ratio values. Therefore, we should pay attention to data processing when estimating Bowen ratio in the future. This will serve as the basis for a fair comparison between observations and models since both are critical measures to better understand the sensible heat and latent heat partitioning.

In conclusion, this analysis provides evidence for the global variations of Bowen ratios among vegetation types and deepens our understanding of energy partitioning which has far-reaching consequences on land and atmosphere interactions. A decrease in Bowen ratio indicates an increasing dominance of latent heat, which could mitigate land surface warming and affect cloud and precipitation processes in the atmosphere (Stoy, 2018; Xu et al., 2020). An increase in Bowen ratio indicates an enhanced surface heating effect, which may aggravate the drought (Schumacher et al., 2019). The spatiotemporal variation of Bowen ratio is the result of both vegetation characteristics and environmental factors (especially climate factors). With global warming, the response of vegetation would play a more important role in modulating energy redistribution (Forzieri et al., 2020). The different vegetation types with their effects on energy partitioning provide the basis for nature-based solutions to mitigate warming. Finally, our data–model comparison emphasizes the importance of accurately representing energy partitioning of vegetation changes in the model, which is critical for studying the climate impacts of land cover change. Therefore, high-quality flux observations are essential for model improvement. In the future, more flux sites are welcome to improve the spatial sampling of the FLUXNET, especially underrepresented vegetation (e.g., deciduous needleleaf forests) and climate types (e.g., extremely dry and cold regions). This combined knowledge from observations and advances in land surface and climate modeling will enhance the credibility of climate predictions and promote better climate policy.

Acknowledgements

This study was supported by the National Key Research and Development Program of China (No. 2017YFA0604701) and the Fundamental Research Funds for the Central Universities.

Author Contribution

Y.L. and H.L. designed the study; H.L. and Y.L. performed the data analysis; H.L., Y.L., and L.Z. analyzed the results; H.L. Y.L. and L.Z. wrote the manuscript.

Data Availability Statement

All code and data needed to reproduce this study are available at Figshare (xxx).

References

1. Baldocchi, D., Falge, E., Gu, L., Olson, R., Hollinger, D., Running, S., Anthoni, P., Bernhofer, C., Davis, K., Evans, R., Fuentes, J., Goldstein, A., Katul, G., Law, B., Lee, X., Malhi, Y., Meyers, T., Munger, W., Oechel, W., Paw, K.T., Pilegaard, K., Schmid, H.P., Valentini, R., Verma, S., Vesala, T., Wilson, K., Wofsy, S., 2001. FLUXNET: A New Tool to Study the Temporal and Spatial Variability of EcosystemScale Carbon Dioxide Water Vapor, and Energy Flux Densities. Bulletin of the American Meteorological Society 82, 2415–2434. https://doi.org/10.1175/1520-0477(2001)082<2415:fantts>2.3.co;2

2. Bateni, S.M., Entekhabi, D., 2012. Relative efficiency of land surface energy balance components. Water Resources Research 48. https://doi.org/10.1029/2011wr011357

3. Boisier, J.P., de Noblet-Ducoudré, N., Pitman, A.J., Cruz, F.T., Delire, C., van den Hurk, B.J.J.M., van der Molen, M.K., Müller, C., Voldoire, A., 2012. Attributing the impacts of land-cover changes in temperate regions on surface temperature and heat fluxes to specific

causes: Results from the first LUCID set of simulations. Journal of Geophysical Research: Atmospheres 117, n/a–n/a. https://doi.org/10.1029/2011jd017106

4. Bonan, G.B., 2008. Forests and Climate Change: Forcings Feedbacks, and the Climate Benefits of Forests. Science 320, 1444–1449. https://doi.org/10.1126/science.1155121

5. Bowen, I.S., 1926. The Ratio of Heat Losses by Conduction and by Evaporation from any Water Surface. Physical Review 27, 779–787. https://doi.org/10.1103/physrev.27.779

6. Burakowski, E., Tawfik, A., Ouimette, A., Lepine, L., Novick, K., Ollinger, S., Zarzycki, C., Bonan, G., 2018. The role of surface roughness albedo, and Bowen ratio on ecosystem energy balance in the Eastern United States. Agricultural and Forest Meteorology 249, 367–376. https://doi.org/10.1016/j.agrformet.2017.11.030

7. Chen, L., Dirmeyer, P.A., Guo, Z., Schultz, N.M., 2018. Pairing FLUXNET sites to validate model representations of land-use/land-cover change. Hydrology and Earth System Sciences 22, 111–125. https://doi.org/10.5194/hess-22-111-2018

8. Cho, J., Oki, T., Yeh, P.J.-F., Kim, W., Kanae, S., Otsuki, K., 2011. On the relationship between the Bowen ratio and the near-surface air temperature. Theoretical and Applied Climatology 108, 135–145. https://doi.org/10.1007/s00704-011-0520-y

9. Cui, W., Chui, T.F.M., 2019. Temporal and spatial variations of energy balance closure across FLUXNET research sites. Agricultural and Forest Meteorology 271, 12–21. https://doi.org/10.1016/j.agrformet.2019.02.026

10. Deng, M., Meng, X., Lyv, Y., Zhao, L., Li, Z., Hu, Z., Jing, H., 2020. Comparison of Soil Water and Heat Transfer Modeling Over the Tibetan Plateau Using Two Community Land Surface Model (CLM) Versions. Journal of Advances in Modeling Earth Systems 12. https://doi.org/10.1029/2020ms002189

11. Duveiller, G., Hooker, J., Cescatti, A., 2018. The mark of vegetation change on Earth's surface energy balance. Nature Communications 9. https://doi.org/10.1038/s41467-017-02810-8

12. Foley, J.A., Costa, M.H., Delire, C., Ramankutty, N., Snyder, P., 2003. Green Surprise? How Terrestrial Ecosystems Could Affect Earths Climate. Frontiers in Ecology and the Environment 1, 38. https://doi.org/10.2307/3867963

13. Forzieri, G., Miralles, D.G., Ciais, P., Alkama, R., Ryu, Y., Duveiller, G., Zhang, K., Robertson, E., Kautz, M., Martens, B., Jiang, C., Arneth, A., Georgievski, G., Li, W., Ceccherini, G., Anthoni, P., Lawrence, P., Wiltshire, A., Pongratz, J., Piao, S., Sitch, S., Goll, D.S., Arora, V.K., Lienert, S., Lombardozzi, D., Kato, E., Nabel, J.E.M.S., Tian, H., Friedlingstein, P., Cescatti, A., 2020. Increased control of vegetation on global terrestrial energy fluxes. Nature Climate Change 10, 356–362. https://doi.org/10.1038/s41558-020-0717-0

14. Gao, X., Avramov, A., Saikawa, E., Schlosser, C.A., 2021. Emulation of Community Land Model Version 5 (CLM5) to Quantify Sensitivity of Soil Moisture to Uncertain Parameters. Journal of Hydrometeorology 22, 259–278. https://doi.org/10.1175/jhm-d-20-0043.1

15. Gholz, H.L., Clark, K.L., 2002. Energy exchange across a chronosequence of slash pine forests in Florida. Agricultural and Forest Meteorology 112, 87–102. https://doi.org/10.1016/s0168-1923(02)00059-x

16. Gray, M.A., McGowan, H.A., Lowry, A.L., Guyot, A., 2018. Surface energy exchanges over contrasting vegetation types on a sub-tropical sand island. Agricultural and Forest Meteorology 249, 81–99. https://doi.org/10.1016/j.agrformet.2017.11.018

17. Jo, Y.-H., Yan, X.-H., Pan, J., Liu, W.T., He, M.-X., 2004. Sensible and latent heat flux in the tropical Pacific from satellite multi-sensor data. Remote Sensing of Environment 90, 166–177. https://doi.org/10.1016/j.rse.2003.12.003

18. Juang, J.-Y., Katul, G., Siqueira, M., Stoy, P., Novick, K., 2007. Separating the effects of albedo from eco-physiological changes on surface temperature along a successional chronosequence in the southeastern United States. Geophysical Research Letters 34. https://doi.org/10.1029/2007gl031296

19. Lawrence, D., Coe, M., Walker, W., Verchot, L., Vandecar, K., 2022. The Unseen Effects of Deforestation: Biophysical Effects on Climate. Frontiers in Forests and Global Change 5. https://doi.org/10.3389/ffgc.2022.756115

20. Lawrence, D.M., Fisher, R.A., Koven, C.D., Oleson, K.W., Swenson, S.C., Bonan, G., Collier, N., Ghimire, B., Kampenhout, L., Kennedy, D., Kluzek, E., Lawrence, P.J., Li, F., Li, H., Lombardozzi, D., Riley, W.J., Sacks, W.J., Shi, M., Vertenstein, M., Wieder, W.R., Xu, C., Ali, A.A., Badger, A.M., Bisht, G., Broeke, M., Brunke, M.A., Burns, S.P., Buzan, J., Clark, M., Craig, A., Dahlin, K., Drewniak, B., Fisher, J.B., Flanner, M., Fox, A.M., Gentine, P., Hoffman, F., Keppel-Aleks, G., Knox, R., Kumar, S., Lenaerts, J., Leung, L.R., Lipscomb, W.H., Lu, Y., Pandey, A., Pelletier, J.D., Perket, J., Randerson, J.T., Ricciuto, D.M., Sanderson, B.M., Slater, A., Subin, Z.M., Tang, J., Thomas, R.Q., Martin, M.V., Zeng, X., 2019. The Community Land Model Version 5: Description of New Features Benchmarking, and Impact of Forcing Uncertainty. Journal of Advances in Modeling Earth Systems 11, 4245–4287. https://doi.org/10.1029/2018ms001583

21. Lee, X., Goulden, M.L., Hollinger, D.Y., Barr, A., Black, T.A., Bohrer, G., Bracho, R., Drake, B., Goldstein, A., Gu, L., Katul, G., Kolb, T., Law, B.E., Margolis, H., Meyers, T., Monson, R., Munger, W., Oren, R., Paw, U.K.T., Richardson, A.D., Schmid, H.P., Staebler,

R., Wofsy, S., Zhao, L., 2011. Observed increase in local cooling effect of deforestation at higher latitudes.. Nature 479, 384–7.

22. Lee, X., Goulden, M.L., Hollinger, D.Y., Barr, A., Black, T.A., Bohrer, G., Bracho, R., Drake, B., Goldstein, A., Gu, L., Katul, G., Kolb, T., Law, B.E., Margolis, H., Meyers, T., Monson, R., Munger, W., Oren, R., U, K.T.P., Richardson, A.D., Schmid, H.P., Staebler, R., Wofsy, S., Zhao, L., 2011. Observed increase in local cooling effect of deforestation at higher latitudes. Nature 479, 384–387. https://doi.org/10.1038/nature10588

23. Ma, Y., Yue, X., Zhou, H., Gong, C., Lei, Y., Tian, C., Cao, Y., 2021. Identifying the dominant climate-driven uncertainties in modeling gross primary productivity. Science of The Total Environment 800, 149518. https://doi.org/10.1016/j.scitotenv.2021.149518

24. Mahrt, L., 1999. Stratified Atmospheric Boundary Layers. Boundary-Layer Meteorology 90, 375–396. https://doi.org/10.1023/a:1001765727956

25. McGloin, R., Šigut, L., Fischer, M., Foltýnová, L., Chawla, S., Trnka, M., Pavelka, M., Marek, M.V., 2019. Available Energy Partitioning During Drought at Two Norway Spruce Forests and a European Beech Forest in Central Europe. Journal of Geophysical Research: Atmospheres 124, 3726–3742. https://doi.org/10.1029/2018jd029490

26. Meier, R., Davin, E.L., Lejeune, Q., Hauser, M., Li, Y., Martens, B., Schultz, N.M., Sterling, S., Thiery, W., 2018. Evaluating and improving the Community Land Models sensitivity to land cover. Biogeosciences 15, 4731–4757. https://doi.org/10.5194/bg-15-4731-2018

27. Morwal, S.B., Narkhedkar, S.G., Padmakumari, B., Maheskumar, R.S., Deshpande, C.G., Kulkarni, J.R., 2016. Intra-seasonal and Inter-annual variability of Bowen Ratio over rain-shadow region of North peninsular India. Theoretical and Applied Climatology 128, 835–844. https://doi.org/10.1007/s00704-016-1745-6

28. Nicholls, E., Carey, S., 2021. Evapotranspiration and energy partitioning across a forest-shrub vegetation gradient in a subarctic alpine catchment. https://doi.org/10.31223/x5m034

29. Oke, T.R., Cleugh, H.A., 1987. Urban heat storage derived as energy balance residuals. Boundary-Layer Meteorology 39, 233–245. https://doi.org/10.1007/bf00116120

30. Pang, G., Chen, D., Wang, X., Lai, H.-W., 2022. Spatiotemporal variations of land surface albedo and associated influencing factors on the Tibetan Plateau. Science of The Total Environment 804, 150100. https://doi.org/10.1016/j.scitotenv.2021.150100

31. Peel, M.C., Finlayson, B.L., McMahon, T.A., 2007. Updated world map of the Köppen-Geiger climate classification. Hydrology and Earth System Sciences 11, 1633–1644. https://doi.org/10.5194/hess-11-1633-2007

32. Ping, Y., Qiang, Z., Yang, Y., Zhang, L., Zhang, H., Hao, X., Sun, X., 2018. Seasonal and inter-annual variability of the Bowen smith ratio over a semi-arid grassland in the Chinese Loess Plateau. Agricultural and Forest Meteorology 252, 99–108. https://doi.org/10.1016/j.agrformet.2018.01.006

33. Qiu, L., Wu, Y., Yu, M., Shi, Z., Yin, X., Song, Y., Sun, K., 2021. Contributions of vegetation restoration and climate change to spatiotemporal variation in the energy budget in the loess plateau of china. Ecological Indicators 127, 107780. https://doi.org/10.1016/j.ecolind.2021.107780

34. Rigden, A.J., Li, D., 2017. Attribution of surface temperature anomalies induced by land use and land cover changes. Geophysical Research Letters 44, 6814–6822. https://doi.org/10.1002/2017gl073811

35. Ryu, Y., Baldocchi, D.D., Ma, S., Hehn, T., 2008. Interannual variability of evapotranspiration and energy exchange over an annual grassland in California. Journal of Geophysical Research 113. https://doi.org/10.1029/2007jd009263

36. Schultz, N.M., Lee, X., Lawrence, P.J., Lawrence, D.M., Zhao, L., 2016. Assessing the use of subgrid land model output to study impacts of land cover change. Journal of Geophysical Research: Atmospheres 121, 6133–6147. https://doi.org/10.1002/2016jd025094

37. Schumacher, D.L., Keune, J., van Heerwaarden, C.C., de Arellano, J.V.-G., Teuling, A.J., Miralles, D.G., 2019. Amplification of mega-heatwaves through heat torrents fuelled by upwind drought. Nature Geoscience 12, 712–717. https://doi.org/10.1038/s41561-019-0431-6

38. Stoy, P.C., 2018. Deforestation intensifies hot days. Nature Climate Change 8, 366–368. https://doi.org/10.1038/s41558-018-0153-6

39. Su, Y., Zhang, C., Chen, X., Liu, L., Ciais, P., Peng, J., Wu, S., Wu, J., Shang, J., Wang, Y., Yuan, W., Yang, Y., Wu, Z., Lafortezza, R., 2021. Aerodynamic resistance and Bowen ratio explain the biophysical effects of forest cover on understory air and soil temperatures at the global scale. Agricultural and Forest Meteorology 308-309, 108615. https://doi.org/10.1016/j.agrformet.2021.108615

40. Tang, Y., Wen, X., Sun, X., Wang, H., 2014. Interannual Variation of the Bowen Ratio in a Subtropical Coniferous Plantation in Southeast China 2003-2012. PLoS ONE 9, e88267. https://doi.org/10.1371/journal.pone.0088267

41. Teuling, A.J., Seneviratne, S.I., Stöckli, R., Reichstein, M., Moors, E., Ciais, P., Luyssaert, S., van den Hurk, B., Ammann, C., Bernhofer, C., Dellwik, E., Gianelle, D., Gielen, B., Grünwald, T., Klumpp, K., Montagnani, L., Moureaux, C., Sottocornola, M., Wohlfahrt, G.,

2010. Contrasting response of European forest and grassland energy exchange to heatwaves. Nature Geoscience 3, 722–727. https://doi.org/10.1038/ngeo950

42. Wang, K., Dickinson, R.E., 2012. A review of global terrestrial evapotranspiration: Observation modeling, climatology, and climatic variability. Reviews of Geophysics 50. https://doi.org/10.1029/2011rg000373

43. Wilson, K., Goldstein, A., Falge, E., Aubinet, M., Baldocchi, D., Berbigier, P., Bernhofer, C., Ceulemans, R., Dolman, H., Field, C., Grelle, A., Ibrom, A., Law, B.E., Kowalski, A., Meyers, T., Moncrieff, J., Monson, R., Oechel, W., Tenhunen, J., Valentini, R., Verma, S., 2002. Energy balance closure at FLUXNET sites. Agricultural and Forest Meteorology 113, 223–243. https://doi.org/10.1016/s0168-1923(02)00109-0

44. Wilson, K.B., Baldocchi, D.D., Aubinet, M., Berbigier, P., Bernhofer, C., Dolman, H., Falge, E., Field, C., Goldstein, A., Granier, A., Grelle, A., Halldor, T., Hollinger, D., Katul, G., Law, B.E., Lindroth, A., Meyers, T., Moncrieff, J., Monson, R., Oechel, W., Tenhunen, J., Valentini, R., Verma, S., Vesala, T., Wofsy, S., 2002. Energy partitioning between latent and sensible heat flux during the warm season at FLUXNET sites. Water Resources Research 38, 30–1–30–11. https://doi.org/10.1029/2001wr000989

45. Xu, X., Jia, G., Zhang, X., Riley, W.J., Xue, Y., 2020. Climate regime shift and forest loss amplify fire in Amazonian forests. Global Change Biology 26, 5874–5885. https://doi.org/10.1111/gcb.15279

46. Yuan, K., Zhu, Q., Zheng, S., Zhao, L., Chen, M., Riley, W.J., Cai, X., Ma, H., Li, F., Wu, H., Chen, L., 2021. Deforestation reshapes land-surface energy-flux partitioning. Environmental Research Letters 16, 024014. https://doi.org/10.1088/1748-9326/abd8f9

538 47. Zeng, S., Xia, J., Chen, X., Zou, L., Du, H., She, D., 2020. Integrated land-surface
539 hydrological and biogeochemical processes in simulating water energy and carbon fluxes
540 over two different ecosystems. Journal of Hydrology 582, 124390.
541 https://doi.org/10.1016/j.jhydrol.2019.124390

542 48. Zhang, M., Wang, J., Li, S., 2019. Tempo-spatial changes and main anthropogenic influence
543 factors of vegetation fractional coverage in a large-scale opencast coal mine area from 1992
544 to 2015. Journal of Cleaner Production 232, 940–952.
545 https://doi.org/10.1016/j.jclepro.2019.05.334

546 49. Zhao, L., Oppenheimer, M., Zhu, Q., Baldwin, J.W., Ebi, K.L., Bou-Zeid, E., Guan, K., Liu,
547 X., 2018. Interactions between urban heat islands and heat waves. Environmental Research
548 Letters 13, 034003. https://doi.org/10.1088/1748-9326/aa9f73

549 50. Van Heerwaarden, C.C., Teuling, A.J., 2014. Disentangling the response of forest and
550 grassland energy exchange to heatwaves under idealized landatmosphere coupling.
551 Biogeosciences 11, 6159–6171. https://doi.org/10.5194/bg-11-6159-2014

552 **Supporting Information**

553 Supplementary Table 1 Vegetation types and time range of the 203 FLUXNET sites used in this
554 study.

Site	IGBP	Range	Site	IGBP	Range	Site	IGBP	Range
BE-Lon	CRO	2004-2014	CA-Qfo	ENF	2003-2010	US-AR1	GRA	2009-2012
CH-Oe2	CRO	2004-2014	CA-SF1	ENF	2003-2006	US-AR2	GRA	2009-2012
DE-Geb	CRO	2001-2014	CA-SF2	ENF	2001-2015	US-ARb	GRA	2005-2006
DE-Kli	CRO	2004-2014	CA-TP1	ENF	2002-2014	US-ARc	GRA	2005-2006
DE-RuS	CRO	2011-2014	CA-TP2	ENF	2002-2007	US-Cop	GRA	2001-2007
DE-Seh	CRO	2007-2010	CA-TP3	ENF	2002-2014	US-Goo	GRA	2002-2006

DK-Fou	CRO	2005-2005	CA-TP4	ENF	2002-2014	US-IB2	GRA	2004-2011
FI-Jok	CRO	2000-2003	CH-Dav	ENF	1997-2014	US-LWW	GRA	1997-1998
FR-Gri	CRO	2004-2014	CN-Qia	ENF	2003-2005	US-SRG	GRA	2008-2014
IT-BCi	CRO	2004-2014	CZ-BK1	ENF	2004-2014	US-Var	GRA	2000-2014
IT-CA2	CRO	2011-2014	DE-Lkb	ENF	2009-2013	US-Wkg	GRA	2004-2014
US-ARM	CRO	2003-2012	DE-Obe	ENF	2008-2014	AR-SLu	MF	2009-2011
US-CRT	CRO	2011-2013	DE-Tha	ENF	1996-2014	BE-Bra	MF	1996-2014
US-Lin	CRO	2009-2010	FI-Hyy	ENF	1996-2014	BE-Vie	MF	1996-2014
US-Ne1	CRO	2001-2013	FI-Let	ENF	2009-2012	CA-Gro	MF	2003-2014
US-Ne2	CRO	2001-2013	FI-Sod	ENF	2001-2014	CH-Lae	MF	2004-2014
US-Ne3	CRO	2001-2013	FR-LBr	ENF	1996-2008	CN-Cha	MF	2003-2005
US-Tw2	CRO	2012-2013	IT-La2	ENF	2000-2002	JP-SMF	MF	2002-2006
US-Tw3	CRO	2013-2014	IT-Lav	ENF	2003-2014	US-PFa	MF	1995-2014
US-Twt	CRO	2009-2014	IT-Ren	ENF	1998-2013	US-Syv	MF	2001-2014
IT-Noe	CSH	2004-2014	IT-SR2	ENF	2013-2014	CA-SF3	OSH	2001-2006
RU-Vrk	CSH	2008-2008	IT-SRo	ENF	1999-2012	ES-Amo	OSH	2007-2012
US-KS2	CSH	2003-2006	NL-Loo	ENF	1996-2014	ES-LgS	OSH	2007-2009
AU-Lox	DBF	2008-2009	RU-Fyo	ENF	1998-2014	ES-LJu	OSH	2004-2013
CA-Oas	DBF	1996-2010	US-Blo	ENF	1997-2007	ES-Ln2	OSH	2009-2009
CA-TPD	DBF	2012-2014	US-GBT	ENF	1999-2006	RU-Cok	OSH	2003-2014
DE-Hai	DBF	2000-2012	US-GLE	ENF	2004-2014	US-SRC	OSH	2008-2014
DE-Lnf	DBF	2002-2012	US-KS1	ENF	2002-2002	US-Sta	OSH	2005-2009
DK-Sor	DBF	1996-2014	US-Me1	ENF	2004-2005	US-Whs	OSH	2007-2014
FR-Fon	DBF	2005-2014	US-Me2	ENF	2002-2014	US-Wi6	OSH	2002-2003
IT-CA1	DBF	2011-2014	US-Me3	ENF	2004-2009	US-Wi7	OSH	2005-2005
IT-CA3	DBF	2011-2014	US-Me5	ENF	2000-2002	AU-ASM	SAV	2010-2014
IT-Col	DBF	1996-2014	US-Me6	ENF	2010-2014	AU-Cpr	SAV	2010-2014
IT-Isp	DBF	2013-2014	US-NR1	ENF	1998-2014	AU-DaS	SAV	2008-2014
IT-PT1	DBF	2002-2004	US-Prr	ENF	2010-2014	AU-Dry	SAV	2008-2014
IT-Ro1	DBF	2000-2008	US-Wi0	ENF	2002-2002	AU-GWW	SAV	2013-2014

IT-Ro2	DBF	2002-2012	US-Wi2	ENF	2003-2003	CG-Tch	SAV	2006-2009
JP-MBF	DBF	2003-2005	US-Wi4	ENF	2002-2005	SD-Dem	SAV	2005-2009
PA-SPn	DBF	2007-2009	US-Wi5	ENF	2004-2004	SN-Dhr	SAV	2010-2013
US-Ha1	DBF	1991-2012	US-Wi9	ENF	2004-2005	ZA-Kru	SAV	2000-2013
US-MMS	DBF	1999-2014	AT-Neu	GRA	2002-2012	AU-Fog	WET	2006-2008
US-Oho	DBF	2004-2013	AU-DaP	GRA	2007-2013	CN-Ha2	WET	2003-2005
US-UMB	DBF	2000-2014	AU-Emr	GRA	2011-2013	CZ-wet	WET	2006-2014
US-UMd	DBF	2007-2014	AU-Rig	GRA	2011-2014	DE-Akm	WET	2009-2014
US-WCr	DBF	1999-2014	AU-Stp	GRA	2008-2014	DE-SfN	WET	2012-2014
US-Wi1	DBF	2003-2003	AU-TTE	GRA	2012-2014	DE-Spw	WET	2010-2014
US-Wi3	DBF	2002-2004	AU-Ync	GRA	2012-2014	DE-Zrk	WET	2013-2014
US-Wi8	DBF	2002-2002	CH-Cha	GRA	2005-2014	FI-Lom	WET	2007-2009
RU-SkP	DNF	2012-2014	CH-Fru	GRA	2005-2014	GL-NuF	WET	2008-2014
AU-Cum	EBF	2012-2014	CH-Oe1	GRA	2002-2008	GL-ZaF	WET	2008-2011
AU-Rob	EBF	2014-2014	CN-Cng	GRA	2007-2010	RU-Che	WET	2002-2005
AU-Tum	EBF	2001-2014	CN-Dan	GRA	2004-2005	SE-St1	WET	2012-2014
AU-Wac	EBF	2005-2008	CN-Du2	GRA	2006-2008	SJ-Adv	WET	2011-2014
AU-Whr	EBF	2011-2014	CN-Du3	GRA	2009-2010	US-Atq	WET	2003-2008
AU-Wom	EBF	2010-2014	CN-HaM	GRA	2002-2004	US-Ivo	WET	2004-2007
BR-Sa1	EBF	2002-2011	CN-Sw2	GRA	2010-2012	US-Los	WET	2000-2014
BR-Sa3	EBF	2000-2004	CZ-BK2	GRA	2004-2012	US-Myb	WET	2010-2014
CN-Din	EBF	2003-2005	DE-Gri	GRA	2004-2014	US-ORv	WET	2011-2011
FR-Pue	EBF	2000-2014	DE-RuR	GRA	2011-2014	US-Tw1	WET	2012-2014
GF-Guy	EBF	2004-2014	DK-Eng	GRA	2005-2008	US-Tw4	WET	2013-2014
GH-Ank	EBF	2011-2014	GL-ZaH	GRA	2000-2014	US-WPT	WET	2011-2013
IT-Cp2	EBF	2012-2014	IT-MBo	GRA	2003-2013	AU-Ade	WSA	2007-2009
IT-Cpz	EBF	1997-2009	IT-Tor	GRA	2008-2014	AU-Gin	WSA	2011-2014
MY-PSO	EBF	2003-2009	NL-Hor	GRA	2004-2011	AU-How	WSA	2001-2014
AR-Vir	ENF	2009-2012	PA-SPs	GRA	2007-2009	AU-RDF	WSA	2011-2013
CA-Man	ENF	1994-2008	RU-Ha1	GRA	2002-2004	US-SRM	WSA	2004-2014

CA-NS1	ENF	2001-2015	RU-Sam	GRA	2002-2014	US-Ton	WSA	2001-2014
CA-Obs	ENF	1997-2010	RU-Tks	GRA	2010-2014	-	-	-

Supplementary Table 2 Conversion of vegetation types between CLM model and IGBP. Due to the lack of wetlands (WET) and deciduous needleleaf forests (DNF) data in the CLM model, no conversion is made. Note: CLM land classification scheme: 1 needleleaf evergreen temperate tree, 2 needleleaf evergreen boreal tree, 3 needleleaf deciduous boreal tree, 4 broadleaf evergreen tropical tree, 5 broadleaf evergreen temperate tree, 6 broadleaf deciduous tropical tree, 7 broadleaf deciduous temperate tree, 8 broadleaf deciduous boreal tree, 9 broadleaf evergreen temperate shrub, 10 broadleaf deciduous temperate shrub, 11 broadleaf deciduous boreal shrub, 12 arctic c3 grass, 13 cool c3 grass, 14 warm c4 grass, 15 crop.

PFT	IGBP
1-2	Evergreen needleleaf forests (ENF)
4-5	Evergreen broadleaf forests (EBF)
6-8	Deciduous broadleaf forests (DBF)
1-8	Mixed forests (MF)
9-11	Closed shrublands (CSH)
9-11	Open shrublands (OSH)
1-11	Woody savannas (WSA)
1-11	Savannas (SAV)
12-14	Grasslands (GRA)
15	Croplands (CRO)

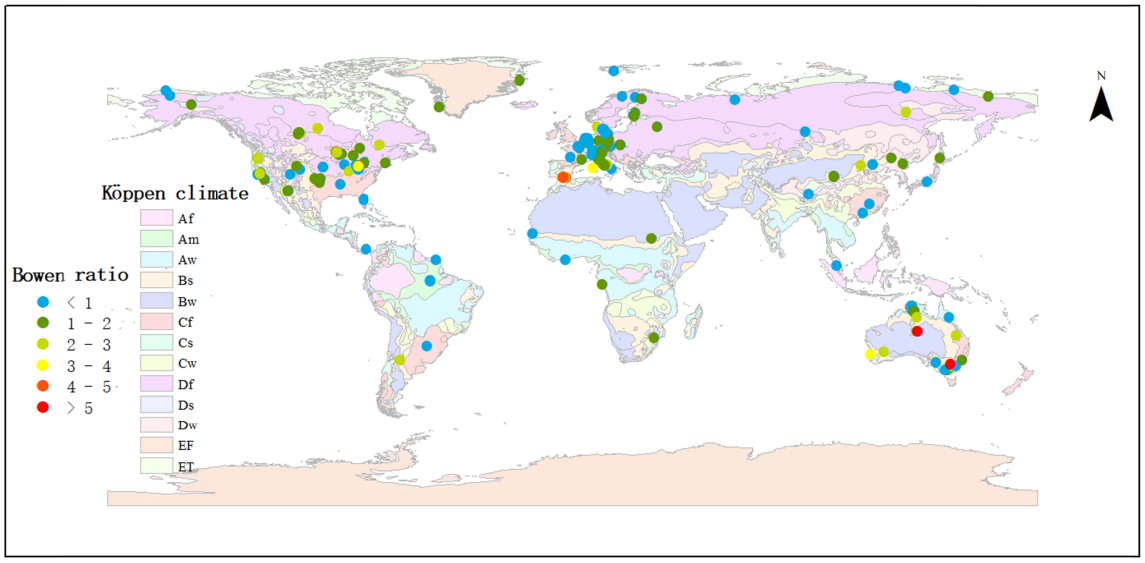

566

571 Supplementary Fig 1 Spatial distribution of multi-year annual mean Bowen ratio across
572 203 FLUXNET sites. Different circles represent FLUXNET sites, colors represent
573 different Bowen ratio, and background colors represent the Köppen climate classification.
574 Take the grassland as an example, the squares are the grassland sites in the northern
575 hemisphere, and the stars are sites in the southern hemisphere.

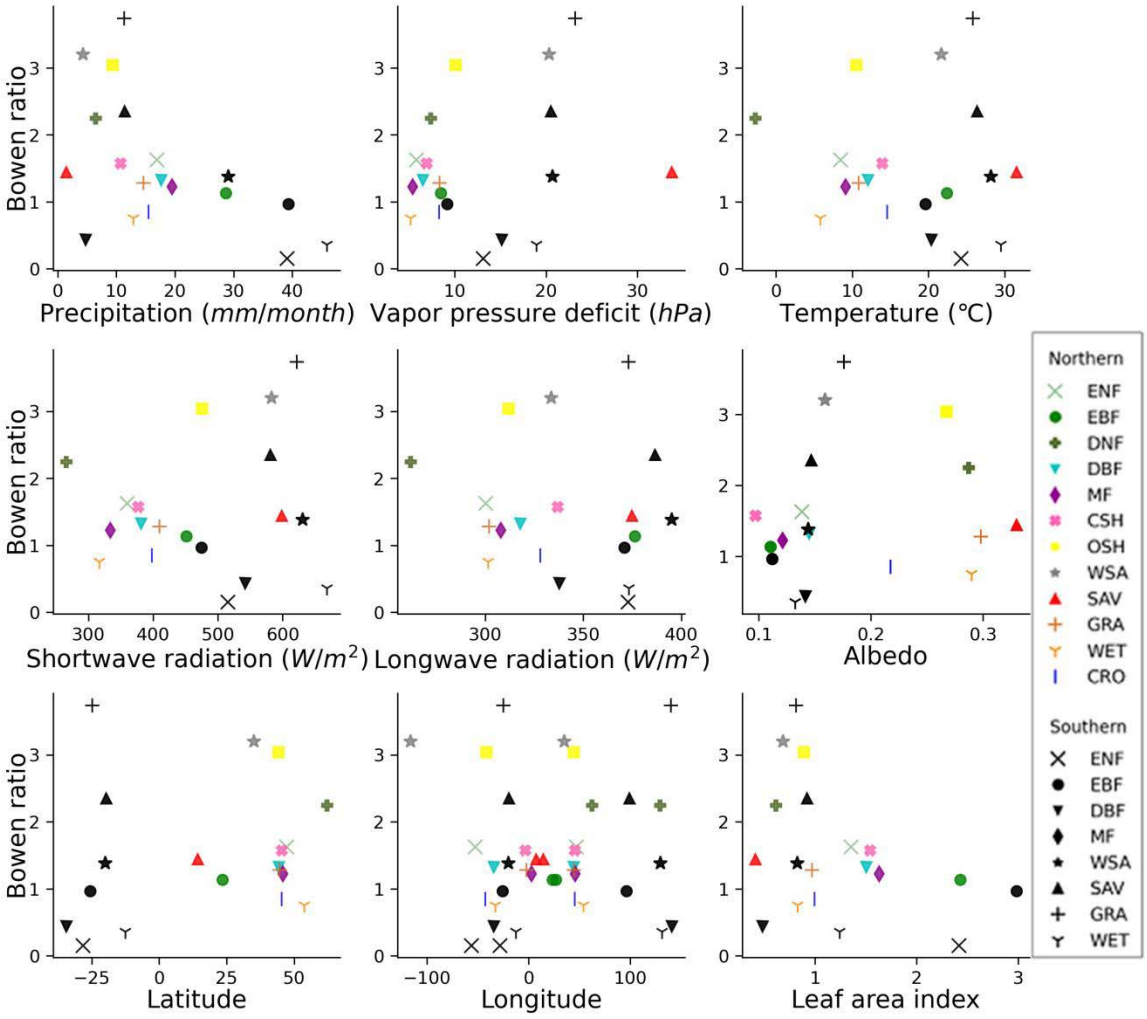

571

572 Supplementary Fig 2 Relationship of Bowen ratio and influencing factors among

573 different vegetation types. Due to data limitations, DNF, CSH, OSH and CRO only have

574 sites in the northern hemisphere.

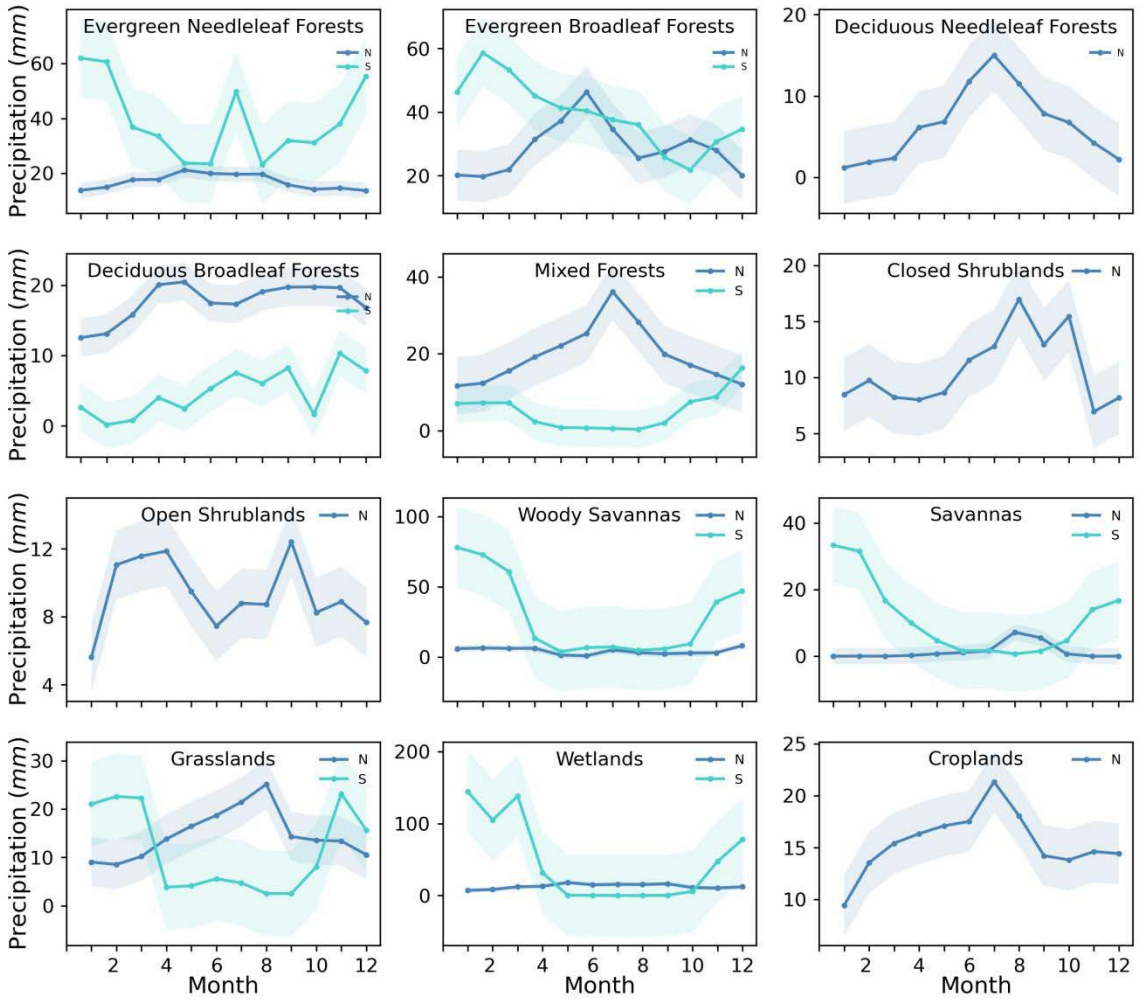

575

576 Supplementary Fig 3 Seasonal variations of precipitation of different vegetation types in
577 the northern (blue) and southern (cyan) hemisphere. The seasonality of SH was shifted by
578 6 months to align it with NH. The shading area represents one standard deviation.

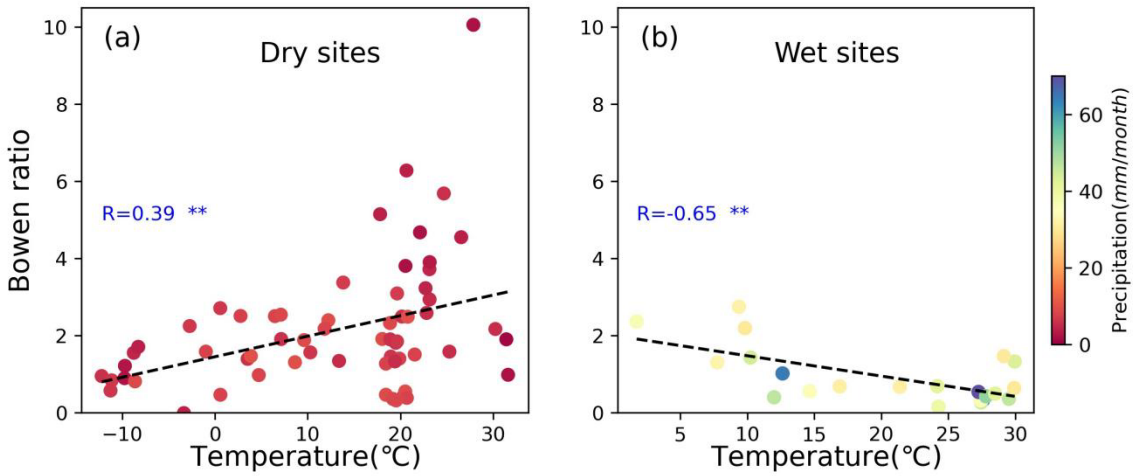

579

580 Supplementary Fig 4 The spatial relationship between Bowen ratio and temperature for

581 dry (precipitation<10mm/month) and wet sites (precipitation>30mm/month) based on

582 FLUXNET data. Each dot represents a site and the dashed lines show the regression line.

583 R is Pearson correlation coefficient with asterisks denoting significance levels (*for

584 p<0.05; **p<0.01, and ***for p<0.001). The color of data points shows the mean

585 precipitation.

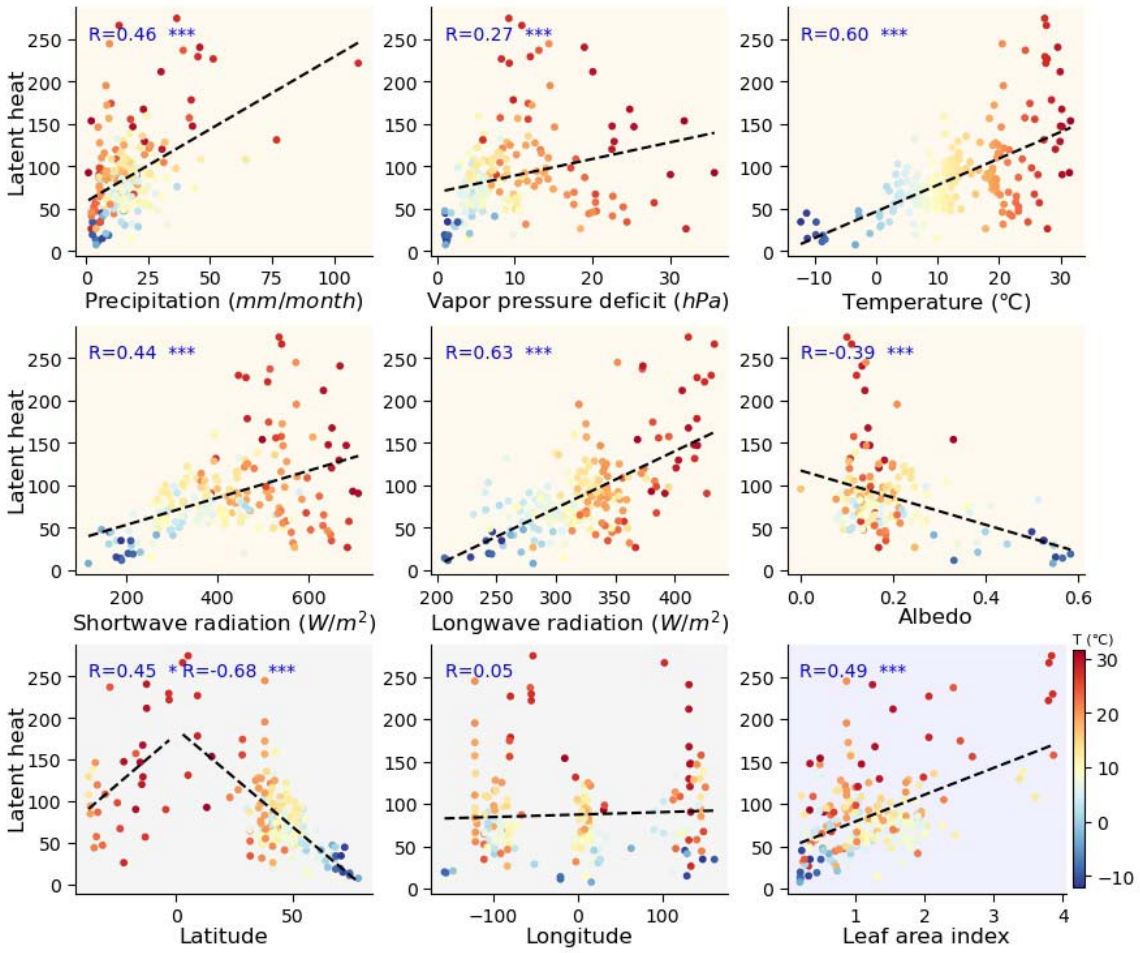

586

587 Supplementary Fig 5 Regression analysis of latent heat flux and different influencing

588 factors. Orange, gray, blue background represent climatic, geography and biological

589 factors. The dashed line shows the regression line. R is Pearson correlation coefficient

590 (*:p<0.05, **: p<0.01, ***: p<0.001). The color of data points shows the mean

591 temperature.

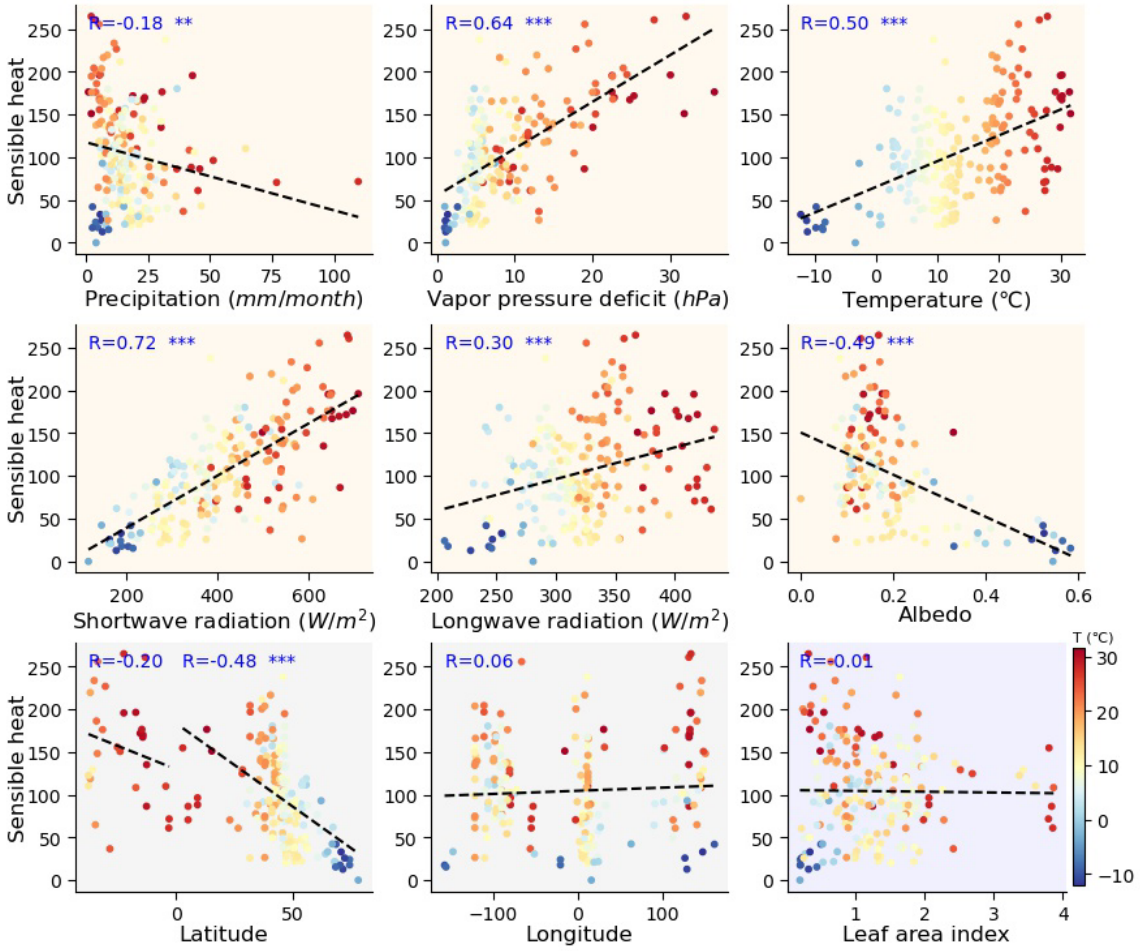

592

593 Supplementary Fig 6 Regression analysis of sensible heat flux and different influencing

594 factors. Orange, gray, blue background represent climatic, geography and biological

595 factors. The dashed line shows the regression line. R is Pearson correlation coefficient

596 (*:p<0.05, **: p<0.01, ***: p<0.001). The color of data points shows the mean

597 temperature.

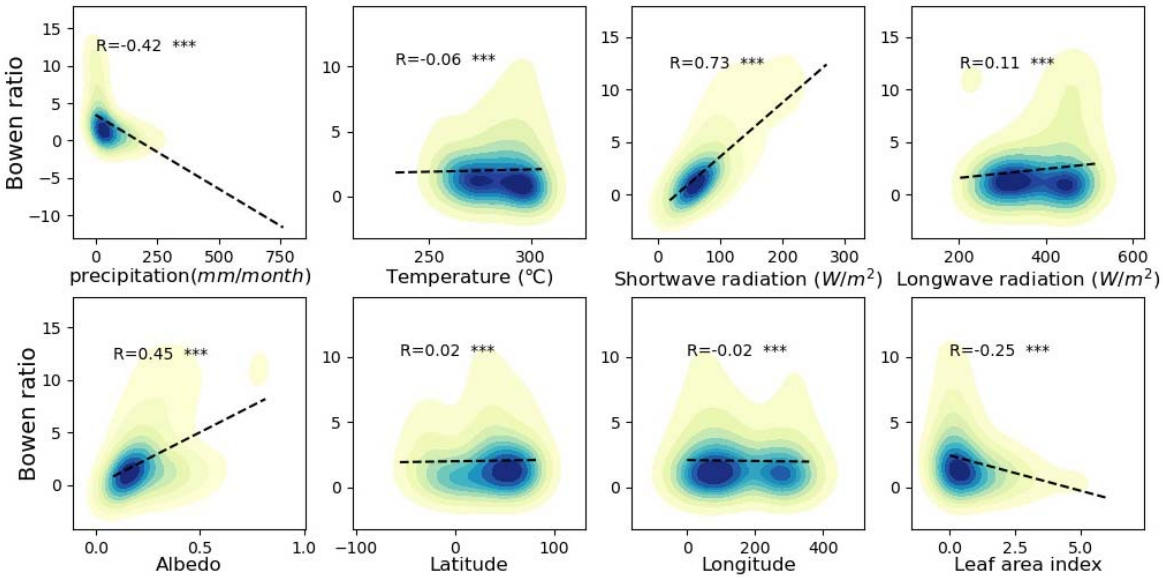

598

599 Supplementary Fig 7 Regression analysis of Bowen ratio and different influencing factors

600 of all grid points in CLM results. The dashed line shows the regression line. R is Pearson

601 correlation coefficient (*:p<0.05, **: p<0.01, ***: p<0.001). Color represents the density

602 of points.

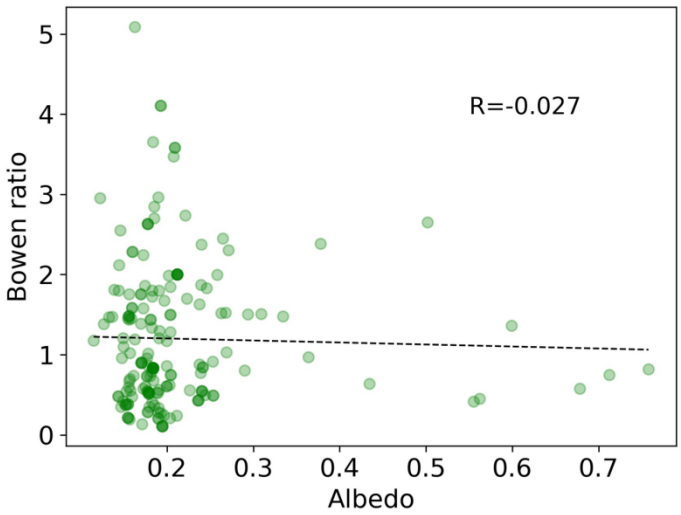

603

604 Supplementary Fig 8 Regression analysis of Bowen ratio and albedo from CLM

605 according to the site locations. P>0.05, implying that there was no significant difference.